

## Inferring the Sun’s Far-side Magnetic-Flux Maps from Far-Side Helioseismic Images through Machine Learning

RUIZHU CHEN,<sup>1</sup> JUNWEI ZHAO,<sup>1</sup> SHEA HESS WEBBER,<sup>1</sup> YANG LIU,<sup>1</sup>  
J. TODD HOEKSEMA,<sup>1</sup> AND MARC L. DEROSA<sup>2</sup>

<sup>1</sup>*W. W. Hansen Experimental Physics Laboratory, Stanford University, Stanford, CA 94305-4085, USA*

<sup>2</sup>*Lockheed Martin Solar and Astrophysics Lab (LMSAL), Palo Alto, CA 94304, USA*

### ABSTRACT

Accurate modeling of the Sun’s coronal magnetic field and solar wind structures require inputs of the solar global magnetic field, including both the near and far sides, but the Sun’s far-side magnetic field cannot be directly observed. However, the Sun’s far-side active regions are routinely monitored by helioseismic imaging methods, which only require continuous near-side observations. It is therefore useful to estimate the far-side magnetic-flux maps using the far-side helioseismic images despite their relatively low spatial resolution and large uncertainties. In this work, we train two machine-learning models to achieve this goal. The first machine-learning training pairs simultaneous *SDO/HMI*-observed magnetic-flux maps and *SDO/AIA*-observed EUV 304 Å images, and the resulting model can convert 304 Å images into magnetic-flux maps. This model is then applied on the *STEREO/EUVI*-observed far-side 304 Å images, available for about 4.3 years, for the far-side magnetic-flux maps. These EUV-converted magnetic-flux maps are then paired with simultaneous far-side helioseismic images for a second machine-learning training, and the trained model can convert far-side helioseismic images into magnetic-flux maps. These helioseismic-image-converted far-side magnetic-flux maps, despite their limitations in spatial resolution and accuracy, can be routinely available on a daily basis, providing useful magnetic information on the Sun’s far side using only the near-side observations.

*Keywords:* Helioseismology — Sun: magnetic fields — solar active regions — space weather

### 1. INTRODUCTION

While solar flares and coronal mass ejections generally have more impacts on space weather, solar wind structures continually impact the heliosphere, affecting near-Earth conditions and influencing the propagation of intense solar events. Prediction of solar wind conditions is therefore a critical aspect of space weather forecasting. However, solar wind models are highly dependent on the global magnetic field on the solar surface as their inner boundary condition, and the lack of observations of the Sun’s far-side magnetic field poses

a significant problem to high-quality space weather forecasting (Nitta & DeRosa 2008; Schrijver & Title 2011). Some global field modelers rely on out-of-date observations for the far-side magnetic field, while others estimate the far-side field through flux-transport models (e.g., Schrijver & DeRosa 2003; Upton & Hathaway 2014). However, active regions (ARs) that emerge on the near side may grow rather than decay after rotating onto the far side, and new ARs may emerge and develop rapidly on the far side of the Sun. These behaviors cannot be modeled by the flux-transport models, causing inaccuracies in the far-side magnetic field data currently used by some global coronal-field and solar wind models. It has been demonstrated by some authors that including far-side magnetic field with updated flux is important to improved modeling of the background solar wind and the solar wind structure. For example, plugging an AR, which emerged on the far side and was detected by a helioseismic far-side imaging method (Lindsey & Braun 2000a), in their ADAPT (Air-Force Data Assimilative Photospheric Flux Transport model; Arge et al. 2010) code, Arge et al. (2013) showed that the modeled solar wind was in better agreement with observations.

For obvious reasons, observations of the Sun's far side are scarce. Carrying a suite of instruments, both spacecraft of the *Solar Terrestrial Relations Observatory* (*STEREO*; Howard et al. 2008) observed the Sun's far side for a few years in extreme ultraviolet (EUV) along with other observables, but without magnetic fields. Now with one spacecraft having lost communications and one approaching the earth, large fraction of the Sun's far side is out of our monitoring scope. On the other hand, local helioseismology techniques were developed to monitor large ARs on the Sun's far side. Lindsey & Braun (2000a) first reported detection of an AR near the Sun's far-side central meridian using a technique called helioseismic holography (Lindsey & Braun 2000b), and this imaging technique was further improved in later endeavors (Braun & Lindsey 2001; Lindsey & Braun 2017). Using time-distance helioseismology technique, Zhao (2007) developed a new far-side imaging code that included both 4- and 5-skip  $p$ -mode waves, and their method was improved as well through follow-up studies (Hartlep et al. 2008; Ionidis et al. 2009). More recently, Zhao et al. (2019) overhauled the time-distance far-side imaging technique by including more multi-skip waves, which resulted in substantial improvements in their reliability of imaging the Sun's far-side ARs. It would be interesting to explore the connections of the far-side helioseismic images with the EUV images as well as magnetic flux on the far side, and the knowledge learned from such connections can then be used to map the Sun's far-side magnetic flux by use of the near-side continuous photospheric observations only.

Actually, the 304 Å observations by *STEREO*/EUVI (Extreme Ultraviolet Imager; Wülser et al. 2004) have already been used to assess the reliability of the helioseismic far-side images. In a series of articles, Liewer et al. (2012, 2014, 2017) compared *STEREO*/EUVI 304 Å images, in which ARs are seen as regions with enhanced emission, with helioseismic holography far-side images, and found that 95% of the helioseismically-detected far-side ARs correspond to an EUV brightening area. Similarly, Zhao et al. (2019) reported that 97.3% of their time-distance helioseismology-detected far-side ARs that exceed a certain

size threshold correspond to a *STEREO*-observed EUV brightening area. *STEREO*/EUVI observations were also used to improve the reliability of helioseismic far-side AR detection. Recently, Felipe & Asensio Ramos (2019) and Broock et al. (2021) trained a machine-learning model that compared the far-side EUV Images and the helioseismic-holography images before these helioseismic images were routinely overlapped for 5 days to enhance the signal-to-noise ratio, and found that the trained model was able to detect with a higher confidence smaller far-side ARs, which would otherwise be unrecognized in the routinely-generated far-side helioseismic images.

Neither the *STEREO*/EUVI observations nor the helioseismic images offer direct magnetic-field information on the far-side ARs; however, past researches seemed to point that both the 304 Å images and the helioseismic images were related to magnetic-field strength, or magnetic flux density, of the ARs. Ugarte-Urra et al. (2015) monitored evolution of total *SDO*/HMI (*Solar Dynamics Observatory* / Helioseismic and Magnetic Imager; Scherrer et al. 2012; Schou et al. 2012) magnetic flux and total *SDO*/AIA (*SDO*/Atmospheric Imaging Assembly; Lemen et al. 2012) 304 Å flux for 10 selected ARs, and found that these two quantities have a power-law relation, indicating that the 304 Å images can be used as a proxy of magnetic flux. Kim et al. (2019) trained a deep-learning code utilizing the *SDO*/HMI magnetograms and *SDO*/AIA 304 Å images, and applied the trained code on the *STEREO*/EUVI 304 Å images to derive the Sun’s far-side magnetic-field maps. For far-side helioseismic images, through comparing the helioseismic phase shifts measured in large and stable far-side ARs with the magnetic-field strengths before and after these ARs’ far-side passages, González Hernández et al. (2007) demonstrated that the far-side ARs’ helioseismic phase shifts, which are the physical quantities displayed in the helioseismic images, are highly correlated with their magnetic strengths.

Based on the substantial progress made by various authors and introduced above, we therefore believe that it is scientifically useful to map the far-side magnetic flux using only the near-side observations, and that it is also practically feasible to do so by combining available observations of near-side magnetic fields, near- and far-side EUV 304 Å images, and far-side helioseismic images through training a couple of machine-learning models. In this work, we train two separate machine-learning models: one model converts EUV 304 Å images into magnetic-flux maps by coupling the near-side *SDO*/HMI magnetic-field observations and *SDO*/AIA 304 Å images; and the other model converts helioseismic far-side images into far-side magnetic-flux maps, with the *STEREO*/EUVI 304 Å images as a bridge between these two sets of conversions. This article is organized as follows: we introduce our analysis procedure and data preparation in Section 2, introduce our first machine-learning code training in Section 3, and the second machine-learning code training in Section 4. We then summarize and discuss our results in Section 5.

## 2. ANALYSIS PROCEDURE AND DATA PREPARATION

### 2.1. Analysis Procedure

112 As demonstrated by [Ugarte-Urra et al. \(2015\)](#), practiced by [Kim et al. \(2019\)](#), and clearly  
 113 seen through comparing Figure 1a and 1c, the Sun's magnetic-field strength and its EUV  
 114 emission, particularly in the wavelength channel of 304 Å, are well correlated, and one  
 115 quantity can be converted to the other, likely with a loss of accuracy. However, when one  
 116 quantity is unavailable, e.g., in this case, the far-side magnetic flux density, a conversion  
 117 with some losses of accuracy is still an acceptable approximation, as long as its limitation is  
 118 recognized and its errors are well estimated. Similar to what [Kim et al. \(2019\)](#) did, in this  
 119 work we plan to train our first machine-learning model using simultaneous observations  
 120 of *SDO/HMI* magnetic-field strengths and *SDO/AIA* 304 Å images, and then apply the  
 121 trained model on the *STEREO/EUVI*-observed far-side 304 Å images for the Sun's far-side  
 122 magnetic-flux maps.

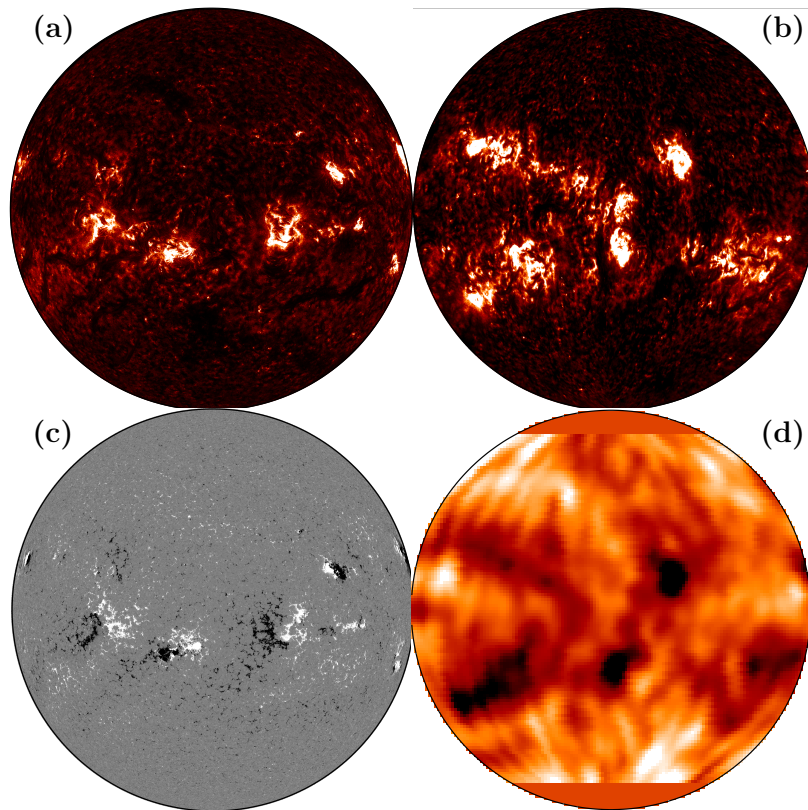


**Figure 1.** Comparison of near-side and far-side images taken at or near 00:00 UT of 2014 March 13. (a) *SDO/AIA*-observed near-side 304 Å image; (b) *STEREO/EUVI*-observed far-side 304 Å image after merging observations from both *STEREO-A* and *STEREO-B* spacecraft. (c) *SDO/HMI*-observed near-side magnetic field; and (d) time–distance helioseismic far-side image obtained from the *SDO/HMI*-observed near-side Dopplergrams. The magnetic field is displayed with a scale of  $-200$  to  $200$  Gauss, the helioseismic image is displayed with a scale of phase shifts from  $-0.10$  to  $0.10$ , and the EUV images are displayed with a DN from 10 to 2000. The *STEREO/EUVI* 304 Å image is displayed after its intensity is calibrated to match the *SDO/AIA* 304 Å level.

123 As demonstrated by [González Hernández et al. \(2007\)](#), the Sun's far-side acoustic phase  
 124 shifts, the physical quantity displayed in helioseismic far-side images, are also well corre-  
 125 lated with magnetic-field strengths. This can also be seen from Figure 1b and 1d, where the

126 locations, sizes, and amplitudes of strong acoustic phase deficits, exhibited as dark patches  
 127 in the figure, seem to show a good correlation with those of the far-side 304 Å brightening  
 128 areas. We therefore plan to train a second machine-learning model by coupling the far-side  
 129 magnetic-flux maps, which are converted from the *STEREO*/EUVI 304 Å images using  
 130 the first trained machine-learning model, and the far-side helioseismic images. The result-  
 131 ing model is expected to be able to convert the far-side helioseismic images into far-side  
 132 magnetic-flux maps.

133 Eventually, this second machine-learning model, together with our time–distance helio-  
 134 seismic far-side imaging model that was previously developed (Zhao et al. 2019), is able  
 135 to generate far-side magnetic-flux maps by merely using continuous near-side full-disk  
 136 Doppler-velocity observations. Such far-side magnetic-flux maps can be routinely pro-  
 137 cessed in *SDO*/HMI’s data-processing pipeline. This is a substantial progress that would  
 138 help the space-weather forecasting and coronal-field modeling, and lower our reliance on  
 139 off-Sun-Earth-line observations for far-side magnetic fields.

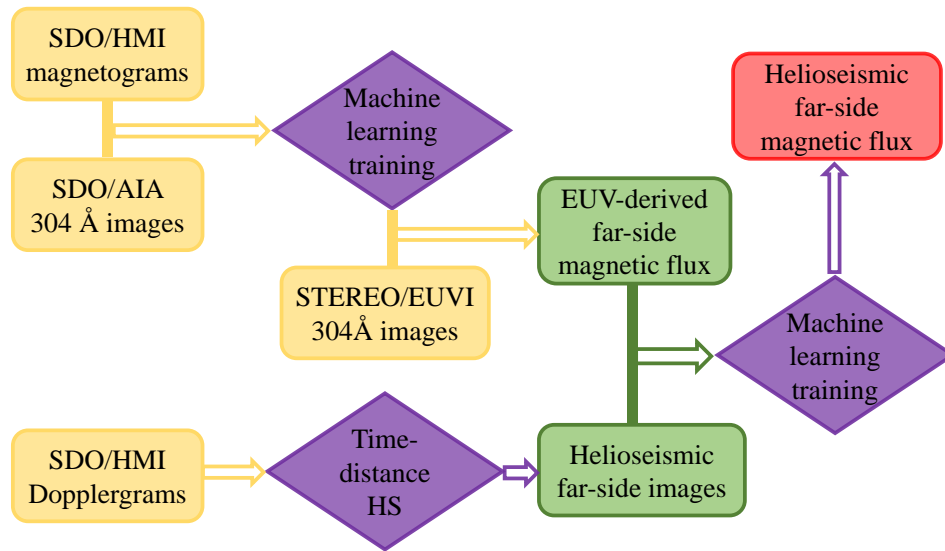


**Figure 2.** Flow chart showing the entire procedure of making far-side magnetic-flux maps using the near-side Doppler-velocity observations. Yellow boxes represent original data inputs, green boxes represent intermediate data products, and red box represents our final data product. Purple diamonds represent the methods that are used in the corresponding processes.

140 Summarizing the analysis procedure prescribed above, Figure 2 presents the flow chart  
 141 of our data preparation, codes developing, and machine-learning training. The original  
 142 data inputs, shown as yellow boxes in this flow chart, include *SDO*/HMI near-side magne-  
 143 tograms and simultaneous *SDO*/AIA near-side 304 Å images, both of which are used in the  
 144 first machine-learning model training; the *SDO*/HMI near-side Dopplergrams will be used  
 145 by a time–distance helioseismic code for the Sun’s far-side helioseismic images; and the  
 146 *STEREO*/EUVI 304 Å images will be used as a bridge to connect the near and far sides.  
 147 The intermediate products, shown as green boxes, include EUV-derived far-side magnetic-

148 flux maps and far-side helioseismic images. Our final data product from this work, shown  
 149 as the red box, is the far-side magnetic-flux maps derived from the helioseismic images.

## 150 2.2. Data Preparation: *SDO/HMI* and *SDO/AIA* Data

151 To prepare the data that are used in our first machine-learning training, for each day  
 152 from 2010 May 1 through 2019 April 30, we take 4 pairs of simultaneously-observed (with  
 153 less than 24 s time difference) *SDO/HMI* line-of-sight magnetograms and *SDO/AIA* 304 Å  
 154 images. A total of  $\sim 13,000$  images are selected during this 9-year period. Corrupted  
 155 images and data captured during flares are excluded. In each calendar year, the data in  
 156 January are not used in the machine-learning training but are kept for testing the trained  
 157 model. More specifically, the data during January 1 and 16, about 4% of the total dataset  
 158 are reserved as the test set for final evaluation, and the data during January 17 and 31 are  
 159 reserved as development set for the performance evaluation in the training process. The  
 160 data between February 16 and December 16, about 83% of the total dataset, are used in  
 161 the machine-learning training. Fifteen days of data before the start and after the end of  
 162 each training data period, i.e., February 1 – 15 and December 17 – 31, are unused in either  
 163 training or testing to avoid the same ARs from appearing in both the training and testing  
 164 sets. The line-of-sight magnetograms are averaged from three consecutive *SDO/HMI* 720 s  
 165 magnetograms, and the 304 Å images are averaged from five consecutive images with a  
 166 24 s cadence. For each pair of images, the off-disk data in the 304 Å image are truncated,  
 167 and both the magnetogram and 304 Å image are rebinned to  $512 \times 512$  pixels and spatially  
 168 aligned, with the alignment accuracy no worse than  $1.0''$ .

169 The *SDO/AIA* 304 Å data need to be recalibrated before being used for the machine-  
 170 learning training. As noted by many authors (e.g., Boerner et al. 2014; Galvez et al. 2019),  
 171 due to the instrumental degradation and the exposure time changes, the flux density in  
 172 the 304 Å images varied substantially with time through the selected 9-year period. The  
 173 *SDO/AIA* team proposed an empirical recalibration method<sup>1</sup> so that the flux density re-  
 174 mains relatively stable. However, the solar spectral irradiance measured by the *SDO/EVE*  
 175 (Extreme Ultraviolet Variability Experiment; Woods et al. 2012) MEGS-A detector, which  
 176 was used for the *SDO/AIA* EUV recalibration, became unavailable after mid-2014 because  
 177 of a power anomaly. While the *SDO/AIA* team afterwards used an alternative scheme in-  
 178 volving the irradiance provided by the Flare Irradiance Spectral Model (Chamberlin et al.  
 179 2007, 2008), we choose to recalibrate the *SDO/AIA* 304 Å intensity by using the *SDO/HMI*  
 180 mean magnetic-flux density. The EUV flux level calibrated before the loss of *SDO/EVE*  
 181 MEGS-A follows a good linear relation with the *SDO/HMI* mean flux, we therefore apply a  
 182 piece-wise empirical correction on the EUV 304 Å flux based on the magnetic-flux density  
 183 after the MEGS-A loss, so that the corrected 304 Å flux follows a same linear relation with  
 184 the magnetic flux throughout the interested period. Figure 3 shows the corrected 304 Å  
 185 mean flux in comparison with the *SDO/HMI*'s mean magnetic-flux density.

<sup>1</sup> <https://www.lmsal.com/sdodocs/doc/dcur/SDOD0060.zip/zip/entry/sdoguidese7.html#x12-600007.6>

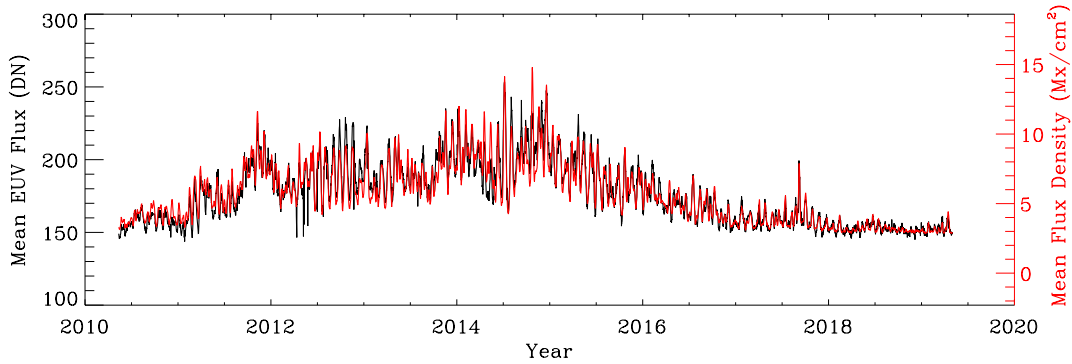


**Figure 3.** Comparison of mean *SDO/AIA* 304 Å flux and mean *SDO/HMI* line-of-sight magnetic flux density, after degradation of the *SDO/AIA* 304 Å data is recalibrated.

2.3. Data Preparation: *STEREO/EUVI* data

186

187

188

189

190

191

192

193

194

195

196

197

198

199

Both *STEREO-A* and *STEREO-B* spacecraft gradually shifted positions relative to the earth as they continued their journey around the Sun. During the period when *STEREO-A*, *STEREO-B* and *SDO/AIA* observations are all available — between 2010 May 13 and 2014 August 16, the combined observations from both *STEREO* spacecraft cover the entire far side of the Sun for most of the time of about 4.3 years. In case of partial coverage that only happened in the first few months, the missing portions are left blank and not used in the training. Many authors combined these data into instantaneous synchronic charts in their analysis, (e.g., [Caplan et al. 2016](#); [Liewer et al. 2017](#); [Zhao et al. 2019](#)); however, in this work, in order to keep these *STEREO/EUVI* images appear similar to the *SDO/AIA* images, i.e., in apparent disk images, so that our first machine-learning trained model can be applied directly on these observations, we keep the *STEREO-A* and *STEREO-B* 304 Å images separately and unchanged as they were observed without any coordinate transformation or image combination.

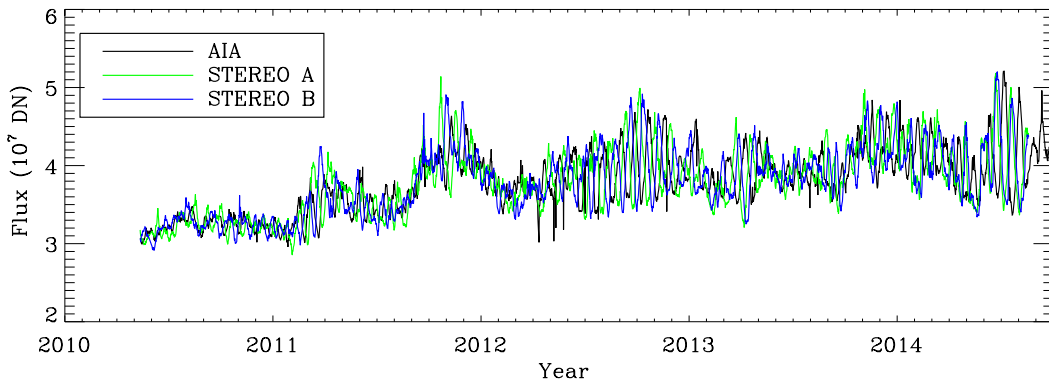


**Figure 4.** Comparison of EUV 304 Å total fluxes observed by the *SDO/AIA* and the two *STEREO/EUVI* instruments during the period of interest, after the *STEREO/EUVI* images are corrected for the instrumental degradation and recalibrated to match *SDO/AIA* values.

200 However, similar to the *SDO/AIA*, both of the *STEREO-A* and *STEREO-B* EUVI instru-  
 201 ments also suffered gradual degradation, and the two instruments might have experienced  
 202 different levels of degradation. Therefore, before these *STEREO/EUVI* 304 Å images can  
 203 be converted into magnetic-flux maps, they also need to be corrected for the degradation;  
 204 and, to keep the data consistent with the *SDO/AIA* observations, these data also need to  
 205 be recalibrated to match the *SDO/AIA* 304 Å flux. In order to carry out such a correction  
 206 and recalibration, we first make 27-day running averages on the *STEREO-A* and *STEREO-*  
 207 *B* and *SDO/AIA* total fluxes. Assuming that the temporal variation of the averaged total  
 208 fluxes is slow and that the total fluxes observed by the three instruments are consistent with  
 209 each other with just a few days of time delay due to different vantage points, we correct  
 210 the degradation of the two *STEREO/EUVI* instruments and recalibrate their 304 Å values  
 211 matching those of the *SDO/AIA* with a time-dependent piece-wise scaling factor. Figure 4  
 212 shows a comparison of our recalibrated *STEREO/EUVI* total fluxes with the *SDO/AIA* to-  
 213 tal flux without the 27-day averaging. These recalibrated *STEREO/EUVI* images are then  
 214 used in our second machine-learning training in Section 4.

#### 215 2.4. Data Preparation: Helioseismic Far-Side Images

216 The far-side helioseismic data used in our second machine-learning training are time-  
 217 distance helioseismic results that are routinely generated by an *SDO/HMI*'s pipeline (Zhao  
 218 et al. 2019). One far-side helioseismic image is calculated every 12 hours using 31-hr-long  
 219 45-sec cadence *SDO/HMI* full-disk Doppler-velocity data. Every far-side helioseismic im-  
 220 age used in this work is an average of seven far-side 12-hr-cadence images, including the  
 221 current one and six immediate prior ones, for a higher signal-to-noise ratio. Due to the  
 222 rotation of the Sun, the far-side west-limb areas are less averaged than the other areas,  
 223 hence being noisier. These far-side images are calculated in longitude – sin(latitude) co-  
 224 ordinate, with a spatial sampling rate of 0.6 pixel<sup>-1</sup>, but the actual spatial resolution of  
 225 such images are believed close to the wavelength of the used helioseismic waves, which is  
 226 around 80 megameters. The time–distance far-side images cover the period of 2010 May  
 227 1 to the present, a total of 12 years with over 8,700 images available; however, due to the  
 228 limitation of *STEREO*'s far-side coverage, only 4.3 years of the data will be used in the  
 229 machine-learning training and testing.

### 230 3. MACHINE-LEARNING MODEL I: CONVERTING EUV IMAGES INTO 231 MAGNETIC-FLUX MAPS

#### 232 3.1. Machine-Learning Training I

233 Our first machine-learning training pairs the near-side observations of magnetic-flux (un-  
 234 signed magnetic-field) maps and EUV 304 Å images that are prepared in Section 2.2. A  
 235 deep convolutional neural network (CNN) model (e.g., Fukushima & Miyake 1982; LeCun  
 236 et al. 1989) will be trained to map a magnetic-flux map to an EUV map, by convolving  
 237 the input magnetic-flux map with a series of convolutional kernels, each of which is fol-  
 238 lowed by a nonlinear mapping. The combination of one convolutional transformation and  
 239 one nonlinear mapping is called one convolutional layer. The machine-learning training

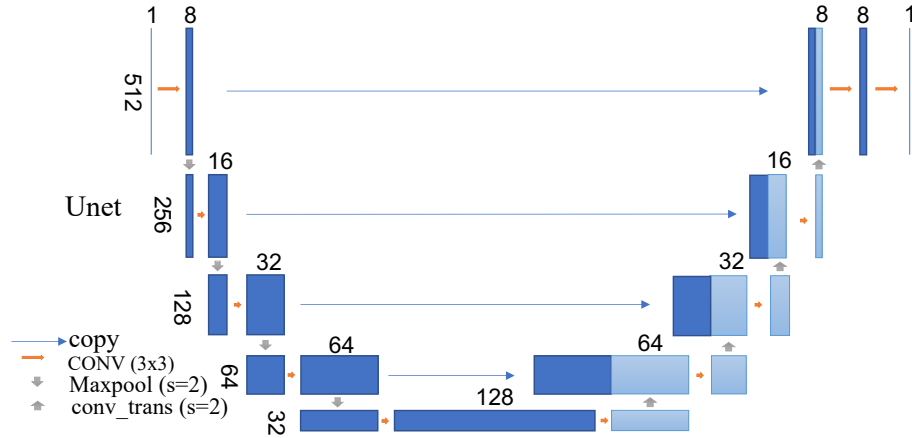


**Figure 5.** Unet deep neural network architecture for the model converting EUV 304 Å images into magnetic-flux maps.

process is an optimization problem to search for optimal kernel values to minimize a loss function, which is defined to quantify the difference between produced maps and target maps. Here we use a CNN with Unet architecture (e.g., [Ronneberger et al. 2015](#)), with its channel number, kernel size, and the image size of each layer illustrated in Figure 5. A rectified linear unit (ReLU) nonlinear mapping is applied after each  $3 \times 3$  convolution, followed by a  $2 \times 2$  maxpool down-sampling. After each down-sampling step, feature channels are doubled. The image is eventually downsized to  $32 \times 32$  pixels with 128 channels, after which convolutional up-sampling is applied. Between each up-sampling step, we concatenate the up-sampled and previously down-sampled channels of the convolutional layer with the same image size, and perform a  $3 \times 3$  convolution followed by a ReLU nonlinear mapping. After each up-sampling step, feature channels are halved. The final output map has same dimensions as the original input map.

Both the *SDO/HMI* magnetic-flux maps and *SDO/AIA* 304 Å images are originally tracked and processed in the form of disk images. However, in the machine-learning training, they are remapped into longitude –  $\sin(\text{latitude})$  coordinate, so that the data fill all of the  $512 \times 512$  grids and margins beyond the solar limb can be removed, which otherwise increases the computational burden without useful scientific returns. This also takes full advantage of the convolutional neural network, avoids artifacts in the convolution across limbs, and preserves better the shapes of ARs when they are close to either of the limbs. Moreover, because the Sun is a sphere, any type of remapping will cause the inhomogeneity of pixel sizes and geometry across the remapped images. The longitude –  $\sin(\text{latitude})$  coordinate is a good choice since it is uniform across longitudes and changes relatively slowly in across latitudes, particularly in the range of active latitudes where this work is more concerned.

We apply gradient descent with Adam algorithm to minimize the loss function ([Kingma & Ba 2014](#)), which is defined as the pixel-to-pixel mean squared error between the prediction images and the target images for the whole training set. The high-flux regions on the images

267 are given a larger weight, since they are the extreme cases of the training data distribution  
 268 and are otherwise less visited in the training. The metrics used for evaluation and selection  
 269 of the trained models are the mean squared errors and the linear correlation coefficients  
 270 between the prediction images and the target images for the development sets, which are  
 271 reserved during the data preparation (Section 2.2).

272

### 3.2. Testing of the Trained Model I

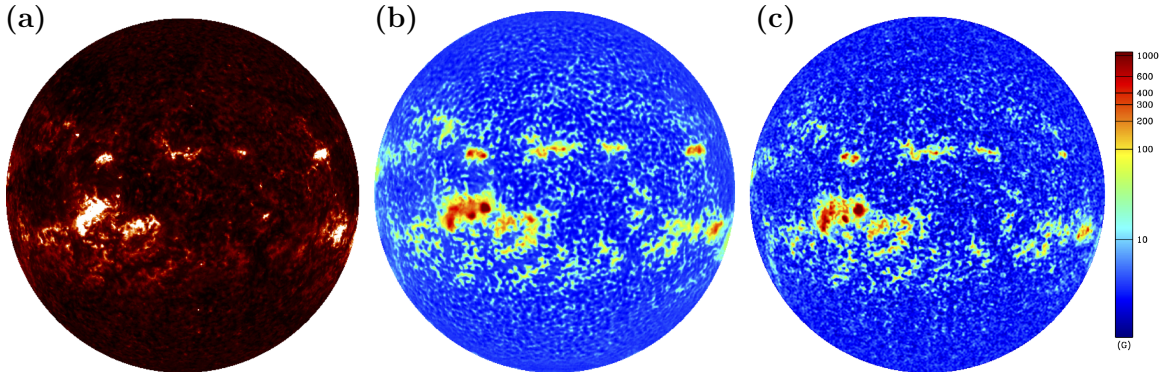


**Figure 6.** (a) An *SDO/AIA* 304 Å image of the Sun, taken at 00:00 UT of 2014 January 6; (b) AI-generated magnetic-flux map based on the 304 Å image shown in panel (a); (c) Simultaneous *SDO/HMI*-observed magnetic-flux map after a  $3 \times 3$  boxcar smoothing for a comparison with panel (b).

273

274

275

276

277

278

279

280

After the machine-learning model is trained, we apply the trained model on the test datasets that are put aside during the data preparation. Figure 6 shows a selected comparison between the AI-generated magnetic-flux map, converted from an *SDO/AIA* 304 Å image, and the simultaneous *SDO/HMI*-observed unsigned magnetic-flux image. It can be seen that, globally, the AI-generated magnetic-flux map has reproduced all magnetic structures that were observed by the *SDO/HMI*, with a one-to-one correspondence; and locally, each active region has similar magnetic structures compared with the observed magnetic-flux map.

281

282

283

284

285

286

287

288

289

While Figure 6 shows the remarkable morphological resemblance between the observed magnetic-flux maps and AI-generated maps, Figure 7 further shows how the values of magnetic-flux densities compare. The scatter plot in Figure 7a shows a pixel-to-pixel comparison of all the test datasets, covering the nine 15-day periods with 4 pairs of datasets each day, after an  $8 \times 8$ -rebin of each image. The correlation coefficient between these rebinned images is as high as 0.88, and the ratio between the two sets of values is close to 1.0. The scatter plot in Figure 7b shows comparison of the globally-averaged mean magnetic-flux densities, obtained for each pair of AI-generated image and directly-observed image. A correlation coefficient of 0.99 is found between these two sets of averaged fluxes.

290

291

292

293

As can be seen from these comparisons, while keeping the general shapes and structures of the EUV 304 Å images, the AI-generated magnetic-flux images show very high correlation with the observed magnetic-flux images in both spatial structures and the values of magnetic flux. Despite the high correlation between the EUV-based AI-generated

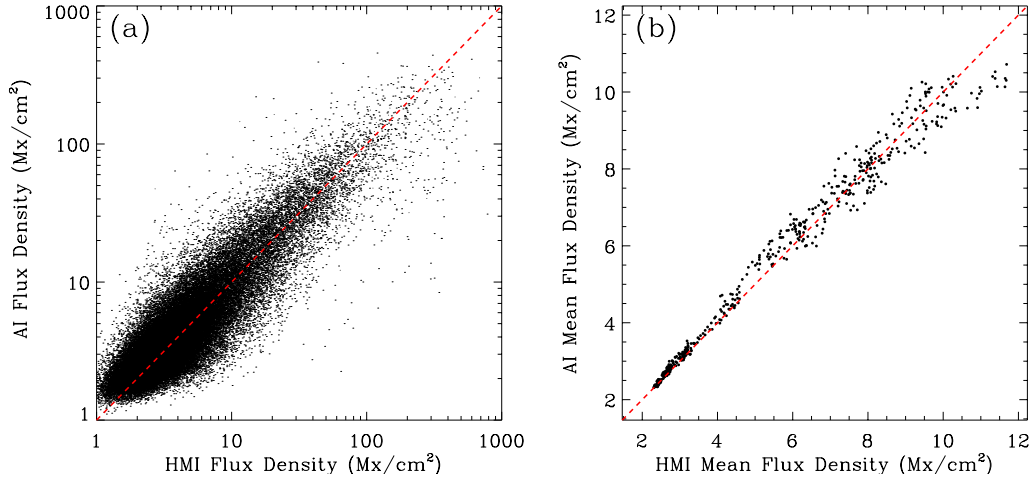


**Figure 7.** (a) Scatter plot comparing the values of magnetic-flux densities from the AI-generated maps and those from the *SDO*/HMI-observed maps. (b) Scatter plot comparing the globally-averaged mean magnetic-flux densities from the AI-generated maps and those computed from the *SDO*/HMI-observed images. One point in the plot represents the results from one image in the test dataset.

294 magnetic-flux maps and the *SDO*/HMI-observed maps, one also needs to recognize that  
 295 in our trained flux maps, the high values often tend to be lower than the observed ones.  
 296 This is probably due to the convolution calculations used in the machine learning, which  
 297 smear out high values and smooth the data. This is also likely due to the EUV flux being  
 298 saturated for strong active regions. Meanwhile, we also need to emphasize that the rela-  
 299 tion between the EUV emission intensity and magnetic-flux density is only an approximate  
 300 power-law relation rather than being a strict one (Ugarte-Urra et al. 2015). Other than that,  
 301 the AI-generated maps are very good proxies to magnetic-flux maps when the latter are not  
 302 directly observable.

303 **3.3. Applying Machine-Trained Model on STEREO/EUVI Data**

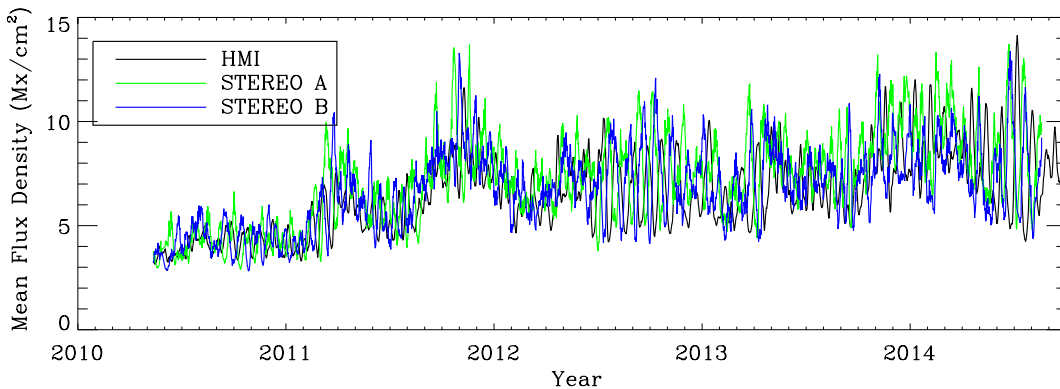


**Figure 8.** Comparing the globally-averaged mean magnetic-flux densities, computed from the *SDO*/HMI-observed magnetic-flux maps and the magnetic-flux maps converted from two sets of *STEREO*-observed 304 Å images.

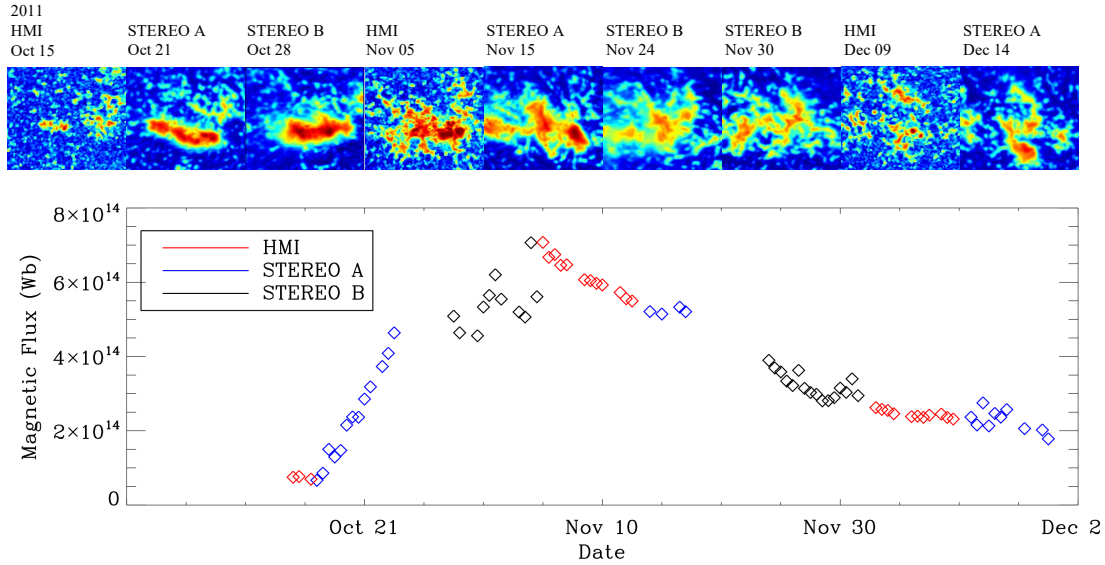


**Figure 9.** Temporal evolution of the total magnetic flux for NOAA AR 11339 during its multiple disk passages on both near and far sides of the Sun.

304 The machine-trained model is then applied on the *STEREO*/EUVI-observed  $304 \text{ \AA}$  im-  
 305 ages, which are prepared separately for the observations by *STEREO-A* and *STEREO-B*  
 306 following prescriptions in Section 2.3. Figure 8 shows a comparison of globally-averaged  
 307 mean magnetic-flux densities, computed from the *SDO*/HMI-observed magnetic-flux maps  
 308 and the magnetic-flux maps converted from the *STEREO-A* and *STEREO-B* images, re-  
 309 spectively, by the machine-trained model with a 12-hr cadence covering the period of May  
 310 2010 to October 2014. These curves are not expected to be identical because they observe  
 311 different parts of the Sun, but their general trends are very similar and their amplitudes  
 312 are also close, demonstrating the reasonableness of our magnetic-flux estimates from the  
 313 *STEREO*-observed  $304 \text{ \AA}$  images.

314 Figure 9 shows another examination of the AI-generated far-side magnetic-flux maps  
 315 — full life of a large active region. The NOAA AR 11339 emerged on the Sun’s near  
 316 side around 2011 October 15, and finally decayed away two months later around 2011  
 317 December 14 on the Sun’s far side. It had three times of near-side disk passage in the  
 318 *SDO*/HMI’s field of view, three passages in the *STEREO-A*’s field of view, and two passages  
 319 in the *STEREO-B*’s field of view. A combination of direct observations and AI-converted  
 320 magnetic-flux maps show the temporal evolution of this region nearly uninterrupted (with  
 321 some exceptions when the AR was near the limbs, i.e.,  $\geq 60^\circ$ , of both *SDO*/HMI and  
 322 *STEREO*/EUVI) for its entire lifetime, and the total flux calculated for this region shows its  
 323 rapid growth and slow decay, associated with sporadic small-scale flux emergence during  
 324 the period. Such a coverage of magnetic-flux maps for a large AR over its entire life span,  
 325 as the one shown in Figure 9, was never achieved before.

#### 326 4. MACHINE-LEARNING MODEL II: CONVERTING HELIOSEISMIC FAR-SIDE 327 IMAGES INTO MAGNETIC-FLUX MAPS

#### 4.1. Preparation of Far-side Magnetic-Flux Maps

Our second machine-learning model is to be trained converting helioseismic far-side images, which are measurements of acoustic waves' phase deficits in and near far-side ARs, into far-side magnetic-flux maps through being paired with the *STEREO*-converted magnetic-flux images obtained in Section 3.3. However, before carrying out this machine-learning training, we need to further process the *STEREO*-converted magnetic-flux maps. The 304 Å images observed by both *SDO/AIA* and the two *STEREO/EUVI* instruments are all affected by the limb-darkening effect as well as disk projections, the former causing the EUV emission intensity gradually lower toward the limbs and the latter affecting the total visible areas and the line-of-sight component of magnetic fields. Because the near-side machine-learning training is done between 304 Å images and line-of-sight magnetic-flux maps without these effect corrections, the *STEREO*-converted magnetic-flux maps carry these limb-darkening and line-of-sight projection effects in the same way as the observed line-of-sight magnetic-flux maps. When combining magnetic-flux maps generated from the two *STEREO* instruments into one far-side magnetic-flux map, the observed disk limbs are often not or even near the limbs of the Sun's far side; therefore corrections are needed to compensate the effects from the limb darkening and the projection. An empirical method, through weighted averaging of seven synthetic far-side magnetic-flux maps as if observed from seven different vantage points, is then developed to make these corrections. However, the detailed process of this correction is beyond the scope of this article, thus is omitted here.

Once the limb-darkening and disk-projection effects are empirically corrected in the *STEREO*-generated magnetic-flux maps, we remap these disk images from the two spacecraft into Carrington coordinate, combine them into one bigger map, and then further crop and transform them into longitude –  $\sin(\text{latitude})$  coordinate to match the helioseismic far-side images with identical scales and grids of  $225 \times 121$ . This coordinate system uses the Sun's apparent disk coordinate instead of the heliographic coordinate, and this way, we do not need to consider effects and coordinate transformations due to the  $B$ -angle variations. Twice every day during the 4.3-year period, two *STEREO*-converted magnetic-flux maps are thus combined into one full far-side image in the new coordinate system. Note that with the continuing movement of both *STEREO* spacecraft, the empirical correction of the flux maps and the merger of two images need to be adjusted accordingly.

Figure 10 shows an example of magnetic-flux maps converted from observations of both *STEREO/EUVI* instruments, the merged far-side flux map from these two separate maps, and the simultaneous helioseismic far-side image. These merged far-side magnetic-flux maps and the helioseismic far-side images in the same coordinate system, as displayed in Figure 10c and 10d, are then used for our second machine-learning training.

#### 4.2. Machine Learning Training II

The far-side magnetic-flux maps, merged together using the AI-generated magnetic-flux maps from both *STEREO/EUVI* observations, are paired together with the far-side helio-

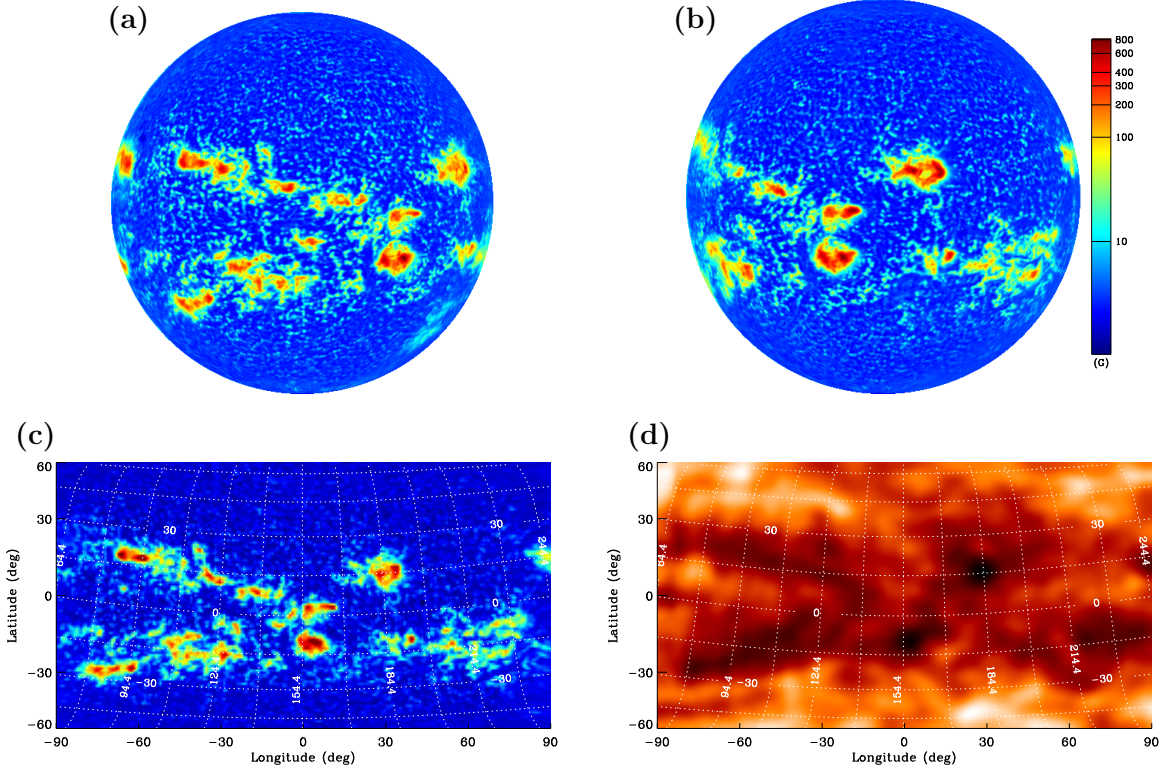


**Figure 10.** (a) Magnetic-flux map converted from *STEREO-A* 304 Å image at 00:00UT of 2014 March 13. (b) Same as panel (a) but for *STEREO-B* converted magnetic-flux map. (c) Far-side magnetic-flux map merged from both maps in panels (a) and (b). (d) Helioseismic far-side image taken at the same time as the map shown in panel (c). Both maps shown in panels (c) and (d) are in the same longitude – sin(latitude) coordinate system, where the longitude and latitude are the apparent disk coordinate. The heliographic coordinates are marked as dashed lines in both panels.

368 seismic images for our second machine-learning training for a model that converts far-side  
 369 helioseismic images into far-side magnetic-flux maps. Two pairs of data are available each  
 370 day covering the period of 4.3 years, totaling about 3,100 pairs of data for our training and  
 371 testing. The data in March of each year, about 8% of the total, are kept for the final testing  
 372 of the model. There are merely 240 pairs of images available for testing, so we do not  
 373 further split the data into the test set and development set as we do for the first machine-  
 374 learning training. Still, 15 days of data immediately before and after the testing period are  
 375 discarded to avoid duplicate active regions in the training and test sets; and the rest of the  
 376 data, about 83% of the total, are used for the machine-learning training.

377 In this machine-learning training, we use a Unet neural network architecture similar to the  
 378 one used in our first training (Section 3.1). However, it should be recognized that although  
 379 the far-side helioseismic images have a temporal cadence of 12 hours, these data are actu-  
 380 ally averaged from 3.5 days of observations, making the effective number of independent  
 381 datasets even smaller. Due to the relatively small training set and the lower dimensionality  
 382 of the images, in this training we use fewer convolutional layers in the framework than  
 383 those used in the first training. The architecture of the neural network is shown in Fig-

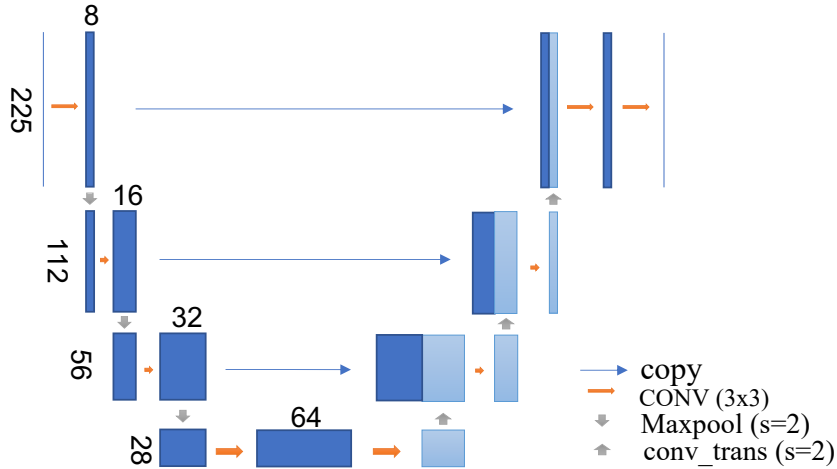


**Figure 11.** Unet deep neural network architecture for the second machine-learning training, converting far-side helioseismic images into magnetic-flux maps.

384 ure 11. The loss function, metrics, and optimization algorithm are chosen to be the same  
 385 as those used in the first neural network training.

386

### 4.3. Testing of the Trained Model II

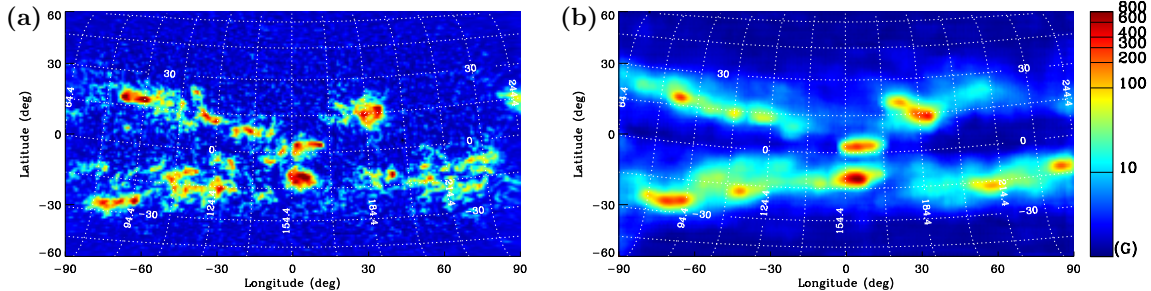


**Figure 12.** Example showing the comparison of (a) *STEREO*-converted far-side magnetic-flux map and (b) helioseismic-image-converted far-side magnetic-flux map, both taken at 00:00 UT of 2014 March 13.

387

388

389

390

391

392

393

394

395

396

After our second machine-learning model is trained, it is applied on the reserved test dataset for a performance evaluation. Figure 12 shows a comparison of a selected *STEREO*-converted magnetic-flux map, which serves as ground truth in this case although they are actually also AI products, and the corresponding helioseismic-image-converted magnetic-flux map. It is worth being reminded that because only low harmonic-degree data are used in the helioseismic-imaging technique, the far-side images obtained from this method often have poor spatial resolution; and the high noises in the helioseismic-imaging method often cause some spurious signals in the far-side images. Therefore, the resultant helioseismic-image-converted magnetic-flux maps have low spatial resolution, and are often associated with spurious regions that may not correspond to a true far-side AR. Nevertheless, the com-

397  
398

parison in Figure 12 shows that the helioseismic-converted flux maps are able to capture most of the large ARs with a reasonable accuracy in the magnetic-flux density values.

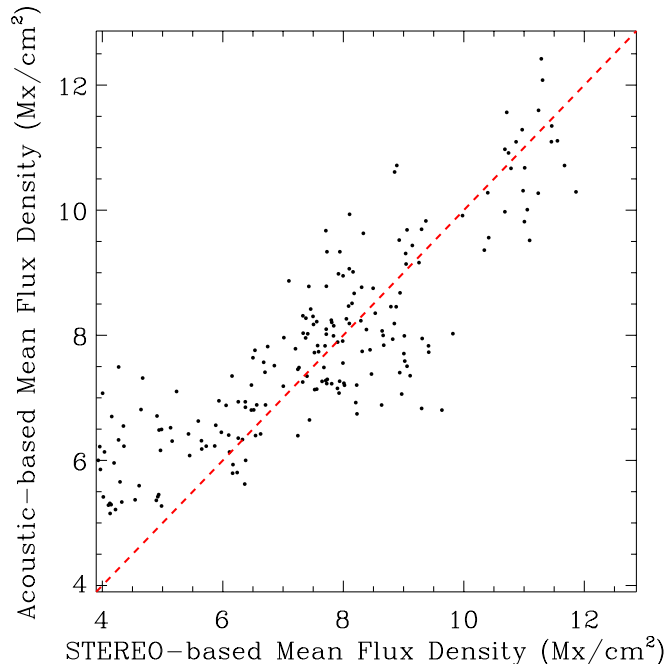


**Figure 13.** Scatter plot comparing the mean magnetic-flux densities from the *STEREO*-generated maps with those from the helioseismic-image-converted maps, both of which are from the test dataset.

399  
400  
401  
402  
403  
404  
405  
406

Figure 13 shows the scatter plot comparing the *STEREO*-converted and the helioseismic-image-converted magnetic fluxes, with each point in the plot averaged from the entire covered far-side area in each test dataset. The mean flux-density values are relatively wide spread, with a correlation coefficient of 0.85 and value ratio close to 1.0 when the mean flux density is above  $6.0 \text{ Mx cm}^{-2}$ . It can be seen that the helioseismic-image-converted magnetic-flux maps are not an accurate reflection of the true far-side magnetic-flux distributions; however, it is undeniable that these maps are still useful approximations when neither far-side magnetic fields nor far-side EUV observations are directly available.

407

## 5. DISCUSSIONS

408  
409  
410  
411  
412  
413

Modeling the Sun’s global-scale coronal magnetic field and solar wind structures requires synchronous photospheric magnetic field on both the Sun’s near and far sides; however, in the foreseeable future, routine observations of the Sun’s far-side magnetic fields are not available. These facts make the far-side magnetic-flux maps, estimated through applying machine-learning methods on helioseismic far-side images, useful for global magnetic field users despite their relatively low spatial resolution and accuracy.

414  
415  
416  
417

In this article, we have demonstrated that it is feasible to use the *STEREO*/EUVI’s  $304 \text{ \AA}$  images to bridge the near- and far-side observations. We have first trained a machine-learning model through pairing the near-side magnetic-field observations and  $304 \text{ \AA}$  images observed by the *SDO* instruments, and satisfactorily converted the  $304 \text{ \AA}$  images into

418 magnetic-flux maps. We then apply the trained machine-learning model on the *STEREO*-  
419 observed 304 Å images for the far-side magnetic-flux maps, which are coupled with the  
420 far-side helioseismic images for a second machine-learning training. The second trained  
421 model is thus able to convert the far-side helioseismic images into magnetic-flux maps. Be-  
422 cause the far-side helioseismic images can be obtained using only the near-side continuous  
423 Doppler-velocity observations, currently available through both space- and ground-based  
424 observations, this is to mean that we are able to map, approximately, the far-side magnetic  
425 flux using only the near-side observations.

426 The resulting far-side magnetic-flux maps are clearly useful to the modeling efforts that  
427 require synchronous near- and far-side magnetic fields as inputs. Particularly, when a rapid  
428 AR emergence occurs on the far side, or when a near-side AR continues to grow sub-  
429 stantially after rotating onto the far side, our data products can provide crucial magnetic  
430 information of the far side that may change the global-scale magnetic configuration. Our  
431 estimated magnetic-flux maps, though usually weaker in peak values, are not much off in  
432 locations and sizes of the ARs.

433 However, there are also clear limits in our far-side magnetic-flux estimates. First, we can  
434 only provide unsigned magnetic-flux density estimates rather than signed magnetic field  
435 estimates. This is because both the 304 Å emission and the helioseismic waves' phase  
436 shifts are only sensitive to magnetic-field strengths, but insensitive to the polarities of the  
437 fields, leaving it unlikely to train a robust machine-learning model that assigns polarities  
438 to the estimated magnetic flux. It is therefore suggested to the potential users of our data  
439 products to assign polarities to the magnetic flux based on Hale's law, i.e., assign the leading  
440 polarity to the leading part of the AR and following polarity to the following part of the AR.  
441 This is certainly a very coarse method. Another way is to couple the flux transport model  
442 (e.g., [Upton & Hathaway 2014](#)) with our magnetic-flux maps, with the former providing  
443 magnetic polarity information and the latter providing total magnetic flux. However, this  
444 method does not work for new emergence on the Sun's far side.

445 Another limit in our far-side magnetic-flux maps is that some small-scale regions, which  
446 appear like small ARs, do not actually correspond to true far-side ARs. This is because the  
447 noise levels are quite high in the helioseismic far-side imaging method. As pointed out by  
448 [Zhao et al. \(2019\)](#), only areas greater than a certain threshold have a probability of 97.3%  
449 corresponding to a true far-side AR. However, on a random far-side map, it is difficult to  
450 tell exactly which region that exceeds the pre-set threshold is actually a true AR; in this  
451 regard, the method developed by [Felipe & Asensio Ramos \(2019\)](#) and [Broock et al. \(2021\)](#)  
452 will likely offer a better guidance on which regions we can have more confidence in and  
453 which ones we cannot.

454 Despite the limitations on our far-side magnetic-flux maps, we still believe that generating  
455 such maps using machine-learning methods is a useful step toward a better modeling of the  
456 Sun's far-side magnetic field without sending a spacecraft there for routine observations.  
457 The quality of these maps can likely be further improved by further refining the helio-

458 seismic far-side imaging technique and, possibly, by further progress of machine-learning  
459 algorithms.

460 Both *SDO* and *STEREO* are NASA missions. *SDO/HMI* is an instrument developed by  
461 Stanford University under a NASA contract, and *SDO/AIA* is an instrument developed by  
462 LMSAL under a NASA contract. The *STEREO/EUVI* synchronic maps are generated by  
463 the *STEREO/SECCHI* team and maintained at JHUAPL, in collaboration with NRL and  
464 JPL. This work was partly sponsored by a NOAA grant NA18NWS4680082.

## REFERENCES

- 465 Arge, C. N., Henney, C. J., Koller, J.,  
466 Compeau, C. R., Young, S., MacKenzie,  
467 D., Fay, A., Harvey, J. W. 2010, AIP Conf.  
468 Proc., 1216, 343
- 469 Arge, C. N., Henney, C. J., Gonzalez  
470 Hernandez, I., Toussaint, W. A., Koller, J.,  
471 Godinez, H. C. 2013, AIP Conf. Proc.,  
472 1539, 11
- 473 Boerner, P. F., Testa, P., Warren, H., Weber,  
474 M. A., & Schrijver, C. J. 2014, SoPh, 289,  
475 2377
- 476 Braun, D. C., & Lindsey, C. 2001, ApJL, 560,  
477 L189
- 478 Broock, E. G., Felipe, T., Asensio Ramos, A.  
479 2021, A&A, 652, A132
- 480 Caplan, R. M., Downs, C., & Linker, J. A.  
481 2016, ApJ, 823, 53
- 482 Chamberlin, P. C., Woods, T. N., & Eparvier,  
483 F. G. 2007, Space Weather, 5, S07005
- 484 Chamberlin, P. C., Woods, T. N., & Eparvier,  
485 F. G. 2008, Space Weather, 6, S05001
- 486 Felipe, T., Asensio Ramos, A., 2019, A&A,  
487 632, A82
- 488 Fukushima, K., & Miyake, S. 1982,  
489 Competition and cooperation in neural nets,  
490 pp. 267-285, Springer, Berlin, Heidelberg.
- 491 Galvez, R., Fouhey, D. F., Jin, M., et al. 2019,  
492 ApJS, 242, 7
- 493 González Hernández, I., Hill, F., & Lindsey,  
494 C. 2007, ApJ, 669, 1382
- 495 Hartlep, T., Zhao, J., Mansour, N. N.,  
496 Kosovichev, A. G. 2008, ApJ, 689, 1373
- 497 Howard, R. A., Moses, J. D., Vourlidas, A., et  
498 al. 2008, SSRv, 136, 67
- 499 Ilonidis, S., Zhao J., & Hartlep, T. 2009,  
500 SoPh, 258, 181
- 501 Kim, T., Park, E., Lee, H., et al. 2019, Nature  
502 Astron, 3, 397
- 503 Kingma, D.P. & Ba, J., 2014. arXiv preprint  
504 arXiv:1412.6980.
- 505 Lemen, J. R., Title, A. M., Akin, D. J., et al.  
506 2012, SoPh, 275, 17
- 507 LeCun, Y., Boser, B., Denker, J., Henderson,  
508 D., Howard, R., Hubbard, W., & Jackel, L.  
509 1989, Advances in neural information  
510 processing systems, 2
- 511 Liewer, P. C., González Hernández, I., Hall, J.  
512 R., Lindsey, C., & Lin, X. 2014, SoPh, 289,  
513 3617
- 514 Liewer, P. C., González Hernández, I., Hall, J.  
515 R., Thompson, W. T., & Misrak, A. 2012,  
516 SoPh, 281, 3
- 517 Liewer, P. C., Qiu, J., & Lindsey, C. 2017,  
518 SoPh, 292, 146
- 519 Lindsey, C., & Braun, D. C. 2000a, Science,  
520 287, 5459
- 521 Lindsey, C., & Braun, D. C. 2000b, SoPh,  
522 192, 261
- 523 Lindsey, C., & Braun, D. C. 2017, Space  
524 Weather, 15, 761
- 525 Nitta, N. V., & DeRosa, M. L. 2008, ApJL,  
526 673, L207
- 527 Ronneberger, O., Fischer, P., & Brox, T. 2015,  
528 In: Navab, N., Hornegger, J., Wells, W.,  
529 Frangi, A. (eds) Medical Image Computing  
530 and Computer-Assisted Intervention –  
531 MICCAI 2015. Lecture Notes in Computer  
532 Science, vol 9351, 234, Springer, Cham.  
533 [https://doi.org/10.1007/978-3-319-24574-  
534 4\\_28](https://doi.org/10.1007/978-3-319-24574-4_28)
- 535 Scherrer, P. H., Schou, J., Bush, R. I., et al.  
536 2012, SoPh, 275, 207

- 537 Schou, J., Scherrer, P. H., Bush, R. I., et al. 547 Woods, T. N., Eparvier, F. G., Hock, R., et al.  
538 2012, *SoPh*, 275, 229 548 *SoPh*, 275, 115
- 539 Schrijver, C. J., & DeRosa, M. L. 2003, *SoPh*, 549 Wülser, J.-P., Lemen, J. R., Tarbell, T. D., et  
540 212, 165 550 al. 2004, *Telescopes and Instrumentation*  
541 Schrijver, C. J., & Title, A. M. 2011, 551 *for Solar Astrophysics*. ed. Fineschi, S.,  
542 *J. Geophys. Res.*, 116, A04108 552 Gummin, M. A. *Proc. SPIE*, v.5171, 111
- 543 Ugarte-Urra, I., Upton, L., Warren, H. P., & 553 Zhao, J. 2007, *ApJL*, 664, L139  
544 Hathaway, D. H. 2015, *ApJ*, 815, 90 554 Zhao, J., Hing, D., Chen, R., & Hess Webber,  
545 Upton, L., & Hathaway, D. H. 2014, *ApJ*, 555 S. 2019, *ApJ*, 887, 216  
546 780, 5